



Quantifying the Relationship between Moreton–Ramsey Waves and “EIT Waves” Using Observations of Four Homologous Wave Events

David M. Long , Jack Jenkins , and Gherardo Valori 

UCL-Mullard Space Science Laboratory, Holmbury St. Mary, Dorking, Surrey, RH5 6NT, UK; david.long@ucl.ac.uk

Received 2019 April 20; revised 2019 July 17; accepted 2019 July 17; published 2019 September 5

Abstract

Freely propagating global waves in the solar atmosphere are commonly observed using extreme ultraviolet passbands (EUV or “EIT waves”), and less regularly in H-alpha (Moreton–Ramsey waves). Despite decades of research, joint observations of EUV and Moreton–Ramsey waves remain rare, complicating efforts to quantify the connection between these phenomena. We present observations of four homologous global waves originating from the same active region between 2014 March 28 and 30 and observed using both EUV and H-alpha data. Each global EUV wave was observed by the *Solar Dynamics Observatory*, with the associated Moreton–Ramsey waves identified using the Global Oscillations Network Group network. All of the global waves exhibit high initial velocity (e.g., 842–1388 km s⁻¹ in the 193 Å passband) and strong deceleration (e.g., –1437 to –782 m s⁻² in the 193 Å passband) in each of the EUV passbands studied, with the EUV wave kinematics exceeding those of the Moreton–Ramsey wave. The density compression ratio of each global wave was estimated using both differential emission measure and intensity variation techniques, with both indicating that the observed waves were weakly shocked with a fast magnetosonic Mach number slightly greater than one. This suggests that, according to current models, the global coronal waves were not strong enough to produce Moreton–Ramsey waves, indicating an alternative explanation for these observations. Instead, we conclude that the evolution of the global waves was restricted by the surrounding coronal magnetic field, in each case producing a downward-angled wavefront propagating toward the north solar pole, which perturbed the chromosphere and was observed as a Moreton–Ramsey wave.

Key words: Sun: activity – Sun: chromosphere – Sun: corona

1. Introduction

Globally propagating waves in the solar atmosphere were first observed in the early 1960s by Moreton (1960) and Moreton & Ramsey (1960) using H α observations of the solar chromosphere. Although these Moreton–Ramsey waves were theorized by Uchida (1968) to be the result of a globally propagating shock wave in the solar corona, this hypothesis could not be tested until the launch of the *Solar and Heliospheric Observatory* (SOHO; Domingo et al. 1995) with its full-Sun Extreme ultraviolet Imaging Telescope (EIT; Delaboudinière et al. 1995) in 1995. The first observations of the so-called “EIT waves” reported by Dere et al. (1997), Moses et al. (1997), and Thompson et al. (1998) were therefore interpreted as the coronal counterpart of the chromospheric Moreton–Ramsey wave.

Despite this initial assumption, discrepancies in the kinematics, morphology, and behavior of these “EIT waves” led to the development of a series of alternative theories contained within two main branches to explain the phenomenon. On the wave branch, in addition to the fast-mode magnetoacoustic wave interpretation originally used, “EIT waves” were alternatively interpreted as slow-mode magnetoacoustic waves (Wang et al. 2009), magnetohydrodynamic solitons (see Wills-Davey et al. 2007) or large-amplitude waves or shocks (see Vršnak & Cliver 2008). The second main branch interpreted “EIT waves” as a signature of magnetic field restructuring during the eruption of a coronal mass ejection (CME), identifying the propagating bright front as being alternatively due to Joule heating at the boundary of a current shell (Delannée et al. 2007, 2008), continuous reconnection with nearby small-scale quiet-Sun loops (Attrill et al. 2007), or

stretching of magnetic field lines during the eruption of the CME (Chen et al. 2002). A full overview of the different theories proposed to explain the “EIT wave” phenomenon may be found in the recent review by Warmuth (2015). More recently, the advent of high temporal and spatial observations across multiple passbands provided by the *Solar Dynamics Observatory* (SDO; Pesnell et al. 2012) spacecraft and the multiple points of view provided by the *Solar Terrestrial Relations Observatory* (STEREO; Kaiser et al. 2008) spacecraft have led to a consensus within the community that “EIT waves” are large-amplitude waves or shocks (see Long et al. 2017a for more details). Note that we shall refer to “EIT waves” as EUV waves for the remainder of this manuscript to highlight the fact that they are observed using instruments other than SOHO/EIT and to ensure consistency in terminology with the Moreton–Ramsey waves observed using the H-alpha passband.

Part of the issue with regard to the uncertainty surrounding the physical interpretation of EUV waves and their relationship to Moreton–Ramsey waves is due to the paucity of simultaneous observations of both phenomena. Although relatively rare, Nitta et al. (2013) identified 171 EUV waves between 2010 April and 2013 January (extended to 362 EUV waves identified between 2010 April and 2016 August by Long et al. 2017b), primarily due to the high synoptic cadence of the Atmospheric Imaging Assembly (AIA; Lemen et al. 2012) on board the SDO spacecraft. However, observations of Moreton–Ramsey waves remain frustratingly rare, despite the worldwide coverage of the Global Oscillations Network Group (GONG) telescope network. Since the launch of SDO in 2010, fewer than five Moreton–Ramsey waves have been identified and

Table 1
List of Events Studied

| Flare Peak Time UT | Flare Source <i>x</i> , <i>y</i> (arcsec) | Flare Size | Angular ^a Extent | Quantity ^b | Kinematics | | | | |
|-------------------------|----------------------------------------------|------------------|--------------------------------|-----------------------|----------------------------|---------------------------|---------------------------|---------------------------|-------------------------|
| | | | | | 171 Å | 193 Å | 211 Å | 304 Å | H α |
| 2014 Mar 28 19:18:00 | 339.3, 286.2 | M2.0 | 326°–43° | vel. acc. | 1044 ± 169 –834 ± 240 | 1011 ± 100 –856 ± 200 | 1025 ± 181 –876 ± 253 | 996 ± 211 –839 ± 355 | 566 ± 66 –589 ± 384 |
| 2014 Mar 28 23:51:00 | 369.9, 284.6 | M2.6 | 320°–19° | vel. acc. | 1498 ± 511 –1662 ± 1130 | 1388 ± 175 –1437 ± 256 | 1404 ± 96 –1458 ± 143 | 1036 ± 143 –1050 ± 481 | 782 ± 57 –1329 ± 374 |
| 2014 Mar 29 17:48:00 | 501.5, 275.9 | X1.0 | 320°–39° | vel. acc. | 1200 ± 140 –1117 ± 178 | 1231 ± 287 –1158 ± 332 | 1215 ± 216 –1148 ± 255 | 974 ± 158 –885 ± 369 | 667 ± 26 –307 ± 93 |
| 2014 Mar 30 11:48:00 | 650.6, 213.8 | N/A ^c | 321°–29° | vel. acc. | 834 ± 81 –803 ± 154 | 842 ± 149 –782 ± 300 | 934 ± 182 –909 ± 379 | 908 ± 200 –976 ± 487 | 444 ± 78 45 ± 542 |

Notes. Note that kinematic errors were calculated by fitting all of the data points shown in Figure 2.

^a Measured clockwise from solar north.

^b Units are km s^{–1} for velocity and m s^{–2} for acceleration

^c Due to a data gap, the peak X-ray flux was not measured by *GOES* for this flare.

analyzed in detail. Asai et al. (2012) reported on a joint Moreton–Ramsey and EUV wave from 2011 August 9 observed using the Solar Magnetic Activity Research Telescope at Hida Observatory, while Francile et al. (2016) reported on a joint Moreton–Ramsey and EUV wave from 2014 March 29 observed using the H-Alpha Solar Telescope for Argentina. Prior to the launch of *SDO*, several authors reported on high-cadence observations of Moreton–Ramsey waves, usually with one or two observations of an associated EUV wave on a similar kinematic trajectory (e.g., Warmuth et al. 2004a, 2004b; Veronig et al. 2006; Balasubramaniam et al. 2010; Muhr et al. 2010).

This discrepancy between the number of global EUV waves and Moreton–Ramsey waves remains a source of ongoing investigation. Independent simulations performed by both Vrřnak et al. (2016) and Krause et al. (2018) suggest that a strong overexpansion of an erupting flux rope during the initial stages of a solar eruption is required to produce a propagating shock wave strong enough to perturb the chromosphere and be observed as a Moreton–Ramsey wave. Vrřnak et al. (2016) suggest that this is a result of the pressure jump associated with the passage of the coronal shock, which produces a downward-propagating quasi-longitudinal MHD shock (well approximated in their model by a switch-on MHD shock). If sufficiently strong, this downward-propagating shock can produce the observed Moreton–Ramsey wave. For weaker events, or if the lateral overexpansion of the flux rope is not sufficiently strong, Vrřnak et al. (2016) suggest that a Moreton–Ramsey wave could still be produced if the eruption is highly asymmetric. Although strong overexpansion of the CME bubble has been previously observed to drive global EUV waves (see Patsourakos et al. 2010; Veronig et al. 2018), it has not yet been observed to drive Moreton–Ramsey waves. However, Moreton–Ramsey waves have traditionally been observed to be arc-shaped and therefore anisotropic (see Warmuth 2015), suggesting that they may be produced by a highly asymmetric eruption. The four events presented here provide the opportunity to test this hypothesis for the relationship between the EUV and Moreton–Ramsey waves, with the EUV waves well observed by *SDO/AIA* and the Moreton–Ramsey waves well observed by the GONG network (albeit using the H-alpha line core rather than the wings).

In this paper, we use observations of four homologous global Moreton–Ramsey and EUV waves that erupted from the same

active region from 2014 March 28 to 30 to quantify the relationship between these phenomena. The observations are presented in Section 2, with the analysis and results presented in Section 3. These results are then discussed in Section 4 before some conclusions are drawn in Section 5.

2. Observations and Data Analysis

The four global wave events studied here are outlined in Table 1 and erupted from NOAA Active Region (AR) 12017 over the course of three days from 2014 March 28 to 30. The different events are shown in Figure 1, with the top row showing running-difference images of the events in the 193 Å passband from *SDO/AIA*, while the bottom row shows the corresponding running-difference H-alpha observations for each event. Each event was associated with a *GOES* X-ray flare, a CME identified by the LASCO CDAW catalog,¹ and a Type II radio burst as measured by NOAA/SWPC.² Table 1 shows that with the exception of the flare on 2014 March 30, which was not measured due to a data gap, all of the flares were quite large, ranging from M2.0 to X1.0.

The events were all well observed by the *SDO/AIA*, with the global EUV waves identifiable in each of the EUV passbands studied. However, only the 171, 193, 211, and 304 Å passbands were used for this analysis as the signal-to-noise was too low in the 94, 131, and 335 Å passbands. In each case, the data were reduced and aligned using the standard SolarSoftWare routines (Freeland & Handy 1998). Although the Coronal Pulse Identification and Tracking Algorithm (CorPITA; Long et al. 2014) was initially applied to the data from each *SDO/AIA* passband to identify and characterize the global EUV wave, it was originally optimized for the 211 Å passband and as a result could not accurately and consistently track the global EUV wave observed in the other passbands. This is due to the significant differences in intensity variation of both the EUV wave and individual features in the surrounding corona in different passbands, all of which can result in the algorithm being unable to consistently identify and track the propagating bright feature. This is a known issue with

¹ https://cdaw.gsfc.nasa.gov/CME_list/UNIVERSAL/2014_03/univ2014_03.html

² See, e.g., https://www.solarmonitor.org/data/2014/03/29/meta/noaa_events_raw_20140329.txt.

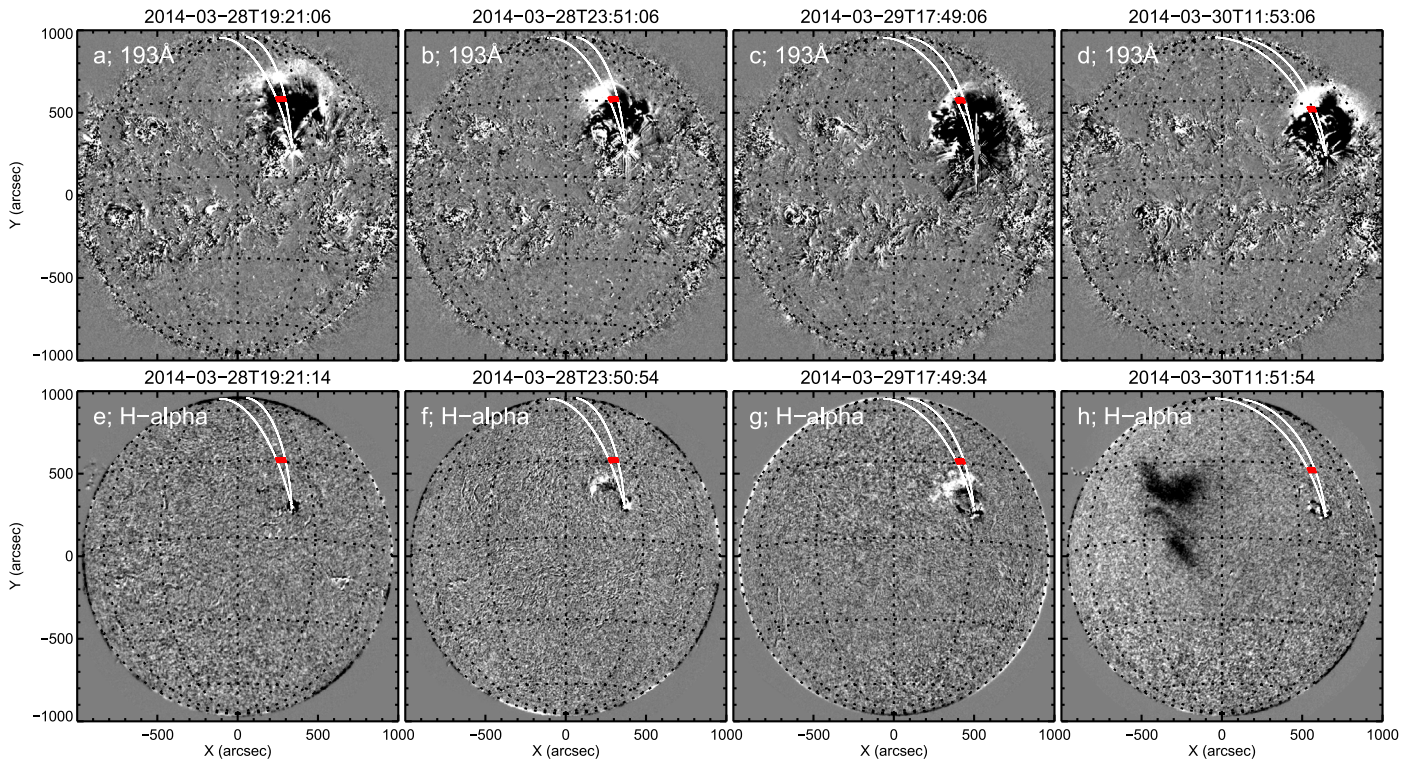


Figure 1. Four global wave events studied in this work. The top row shows the events observed using the 193 \AA passband on *SDO/AIA*, while the bottom row shows the same events as observed using the GONG $H\alpha$ passband. Each panel shows a running-difference image, with the leading image taken at the time shown and the following image 120 s earlier. The red region shows the location used to estimate the variation in density and temperature in Section 3.2.

CorPITA, and one that the code is currently being updated to try and overcome.

Instead, the intensity profiles derived by CorPITA were combined to produce a series of distance–time stack plots which were then used to manually identify the leading edge of the EUV wave with time for each passband studied. Each panel in Figure 1 shows the white arc sectors used to make the stack plots shown in Figure 2. This approach was used to ensure consistency between passbands and events and enable the systematic calculation of errors when estimating the kinematics shown in Table 1. The EUV waves were then manually identified by selecting the leading edge of the bright feature in each arc sector for each passband and each event using 100 data points. This process was repeated five times for each arc sector to minimize user bias and ensure an accurate identification of the front. The kinematics were then estimated for each arc sector using a quadratic model applied to all 500 data points, with the mean initial velocity and acceleration values for each passband listed in Table 1.

In addition to the EUV observations obtained by *SDO/AIA*, all four of the events were also observed in the $H\alpha$ passband by the GONG network of $H\alpha$ telescopes. The GONG network consists of a series of six telescopes located around the world at Learmonth Solar Observatory in Western Australia, Big Bear Solar Observatory in California, USA, the High Altitude Observatory on Mauna Loa in Hawaii, USA, Udaipur Solar Observatory in India, the Observatorio del Teide in the Canary Islands and the Cerro Tololo Interamerican Observatory in Chile. Each of the different Moreton–Ramsey wave events were observed by a combination of telescopes, complicating the resulting analysis due to variations in seeing conditions. Although the Moreton–Ramsey waves could be

visually identified using movies, they are harder to identify in individual images and indeed in the stack plots (as shown in Figure 2) as a result of this discrepancy between observatories. This was overcome by treating the data from each observatory independently and then combining the processed images to identify the Moreton–Ramsey waves.

The data from each GONG observatory were aligned by first aligning the single image with the best seeing conditions identified by-eye closest in time to the flare to the relevant image from the 304 \AA passband observed by *SDO/AIA*. Angular variations between different GONG observatories were then accounted for by deprojecting the subsequent images to polar coordinates and using different features to ensure accurate cross-correlation between all of the images. Each image for a given GONG observatory was then normalized with respect to the first image to ensure a consistent intensity range and to counteract variations in intensity due to atmospheric seeing. As a result of this procedure of first aligning a GONG image to an AIA image and then aligning all subsequent GONG images to the initial aligned image, the same arc sectors could be used to estimate kinematics from all of the EUV and GONG images. A base difference approach (i.e., subtracting the first image from all subsequent images for each observatory) was then used to identify the Moreton–Ramsey wave in both stack plots (see Figure 2) and individual intensity profiles (see Figure 3).

3. Results

3.1. Pulse Characteristics

The events described here displayed similar characteristic behavior, propagating anisotropically away from the erupting

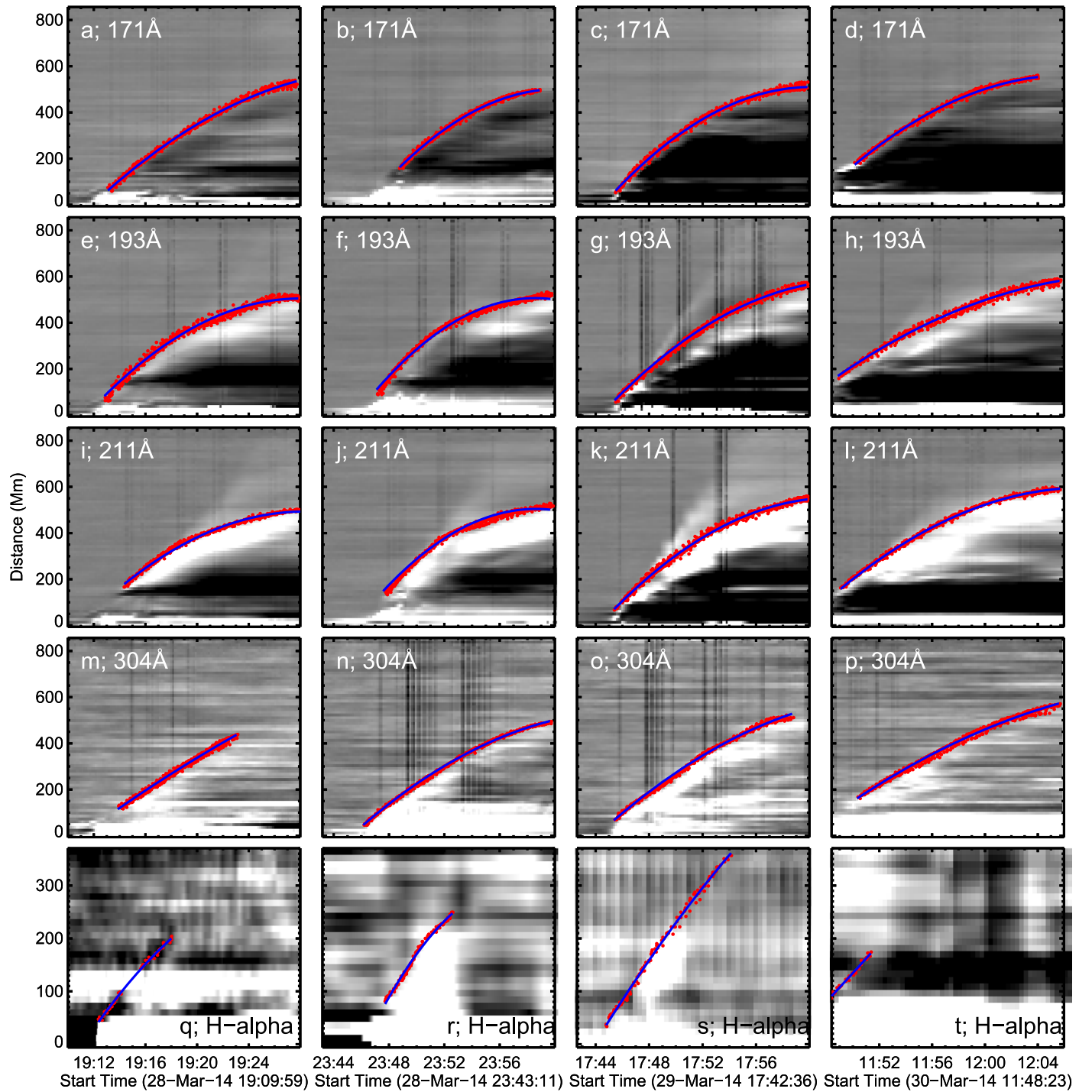


Figure 2. Stack plots showing the variation in base difference intensity along an arc sector directed toward solar north in the 171, 193, 211, 304 Å and H α passbands for each of the four events studied. In each case, the data points indicating the manual selection of the wavefronts are shown in red, the best-fit kinematics are indicated by the solid blue lines, and the mean values across all arc sectors are given in Table 1. Note that while the global waves are easily identifiable in the four EUV passbands, they are much fainter in the H α passband, with the waves in panels (q) and (t) being dark instead of bright. We believe that this is most likely due to the dynamics of the chromospheric plasma contributing to the H-alpha line. Although two intensity increases can be observed for each event in the 193 and 211 Å passbands, the bright, slow feature is identified here as the global wave, whereas the faint, fast feature departing tangentially from the blue fit is the shock associated with the erupting coronal mass ejection previously identified by Francile et al. (2016). While the fits to the 193 and 211 Å data in panels (f) and (j) turn over before the end time, this is unphysical and indicates that the fits in these cases have significant uncertainties. The increased uncertainty in these particular fits is accounted for in Table 1, which gives the mean initial velocity and acceleration for all arcs across the full angular extent of the EUV waves.

active region toward solar north with a comparable angular extent (as shown in Figure 1 and outlined in Table 1). However, in contrast to the short time periods over which the events previously studied by Kienreich et al. (2011, 2013) and Zheng et al. (2012) occurred (≈ 10 hr, ≈ 12 hr, and ≈ 3 hr

respectively), the four events studied here occurred over the course of ≈ 42 hr between 19:00 UT on 2014 March 28 and 13:00 UT on 2014 March 30, suggesting some long-lasting property of the environment where the wave propagation took place. In addition, although ≈ 20 flares erupted from this active

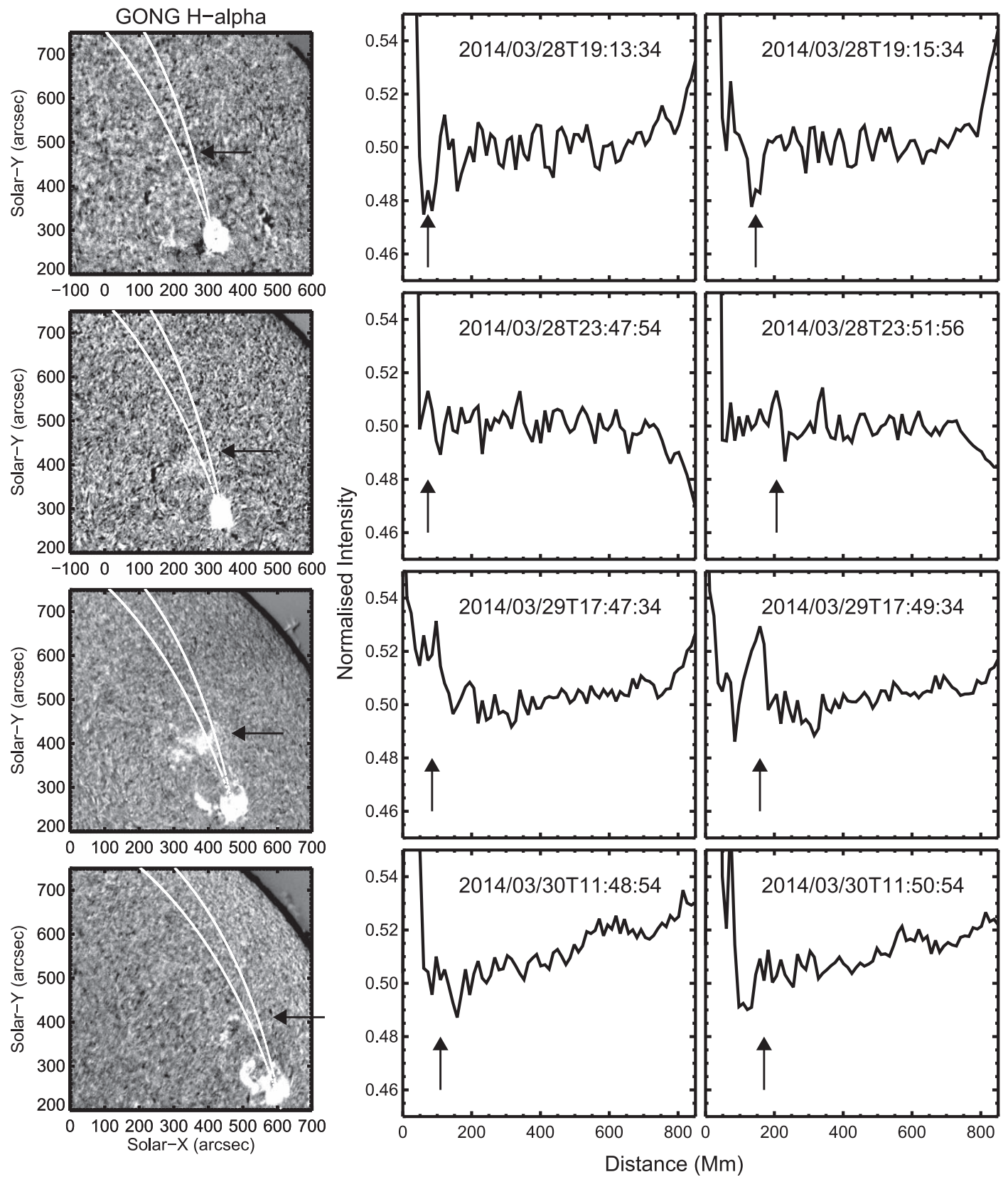


Figure 3. Intensity images (left column) and intensity plots (center and right columns) showing the Moreton–Ramsey waves associated with each of the four events studied here. Arrows in each column indicate the positions of the identified Moreton–Ramsey waves. Note that the Moreton–Ramsey waves manifest as an increase in intensity for the bottom three events but as a decrease in intensity for the top event. Although this is most likely due to the H-alpha line being shifted due to the down-up swing typically associated with Moreton–Ramsey wave observations, it is not possible to confirm this hypothesis without observations from the H-alpha line wings, which are not available for these events.

region over the same time period,³ only the four events studied here were associated with global waves, suggesting a common initiation process. All four events were also seen to originate from the same part of the active region on its northern side, suggesting a homologous nature in the triggering mechanism and property of the erupting structure. The four events can therefore be considered to share comparable geometrical properties and to originate and behave in a similar manner (see Kienreich et al. 2011, 2013; Zheng et al. 2012).

Note that following the work of Francile et al. (2016), the lower, more intense feature observed in the second and third rows of Figure 2 (corresponding to the on-disk global wave rather than the projection of the erupting CME) was used to estimate the kinematics of the global wave in the 193 and 211 Å passbands. Although the global waves were quite clear in the different EUV passbands with minimal processing (as seen in Figure 1), the associated Moreton–Ramsey waves were much more difficult to identify in the H-alpha passbands. However, following the processing approach outlined in Section 2, it was possible to identify a leading edge in each case which could then be fitted to estimate the kinematics.

Each of the EUV wave events studied here can be seen from Table 1 to have had a high initial velocity with strong negative acceleration. Although no clear correlation can be observed between the flare intensity and the kinematics of the EUV wave, this is not unexpected as was previously discussed by Long et al. (2017b). In fact, the average wave speed was higher for event 2 (with its M2.6 flare) than for event 3 (with its X1.0 flare), despite the smaller time gap between events 1 and 2 compared to events 2 and 3. The average EUV wave initial velocities (particularly in the commonly used 193 and 211 Å passbands) are comparable with other EUV wave events observed using *SDO* (see Nitta et al. 2013; Long et al. 2017b). Although the kinematics estimated using the 304 Å passband are lower than the other three EUV passbands, this is consistent with previous observations (see Long et al. 2008).

The Moreton–Ramsey waves studied here were first identified “by-eye” using images taken in the line core of the H-alpha line by the GONG observatories. Although apparent in moving images due to the ability of the human eye to detect motion, the Moreton–Ramsey waves were much more difficult to identify in individual images. Figure 3 shows a combination of still images (left column) with arc sectors along which the intensity could be taken to try and identify the waves (center and right columns). The arrows in each of the plots in the center and right columns indicate the Moreton–Ramsey wave, enabling its temporal evolution to be tracked. As the Moreton–Ramsey waves were quite difficult to identify for each event, the intensity variation in the intensity profile plots corresponding to the Moreton–Ramsey wave was identified by moving back and forth between consecutive images and intensity profiles to determine a moving feature. The evolution of the Moreton–Ramsey wave was shown in the stack plot shown in Figure 2 by scaling the stack plot to highlight a sloping feature (indicative of a propagating front) and then manually identifying the leading edge of that sloping feature using a point-and-click approach (producing the points shown in panels (q)–(t) of Figure 2). This approach enabled the features identified by the arrows in Figure 3 to be determined

and matched to the features identified in the bottom row of Figure 2.

These intensity plots at each moment in time could then be combined to produce the stack plots shown in the bottom row of Figure 2, enabling a determination of the temporal evolution of the Moreton–Ramsey waves for each event. As with the estimation of the kinematics for the EUV waves, the Moreton–Ramsey wave kinematics were estimated by repeating the identification of the leading edge of the propagating front five times and fitting the resulting cloud of data points with a quadratic function to estimate the initial velocity and acceleration. In contrast to previously studied events, the Moreton–Ramsey waves identified here were found to be much slower than the associated global EUV waves. However, this may be a function of the lower cadence H-alpha observations (20–60 s) compared to the EUV observations (12 s) (see Byrne et al. 2013), and the difficulty in identifying the Moreton–Ramsey waves in the H-alpha observations. Moreton–Ramsey waves are thought to be the result of a coronal wave pressing down on the chromosphere, making them easier to observe using the wings of H-alpha due to a characteristic down–up swing in Doppler velocity. However, the downward force exerted by the coronal wave would need to be particularly large to be observed in line core images. This is not always the case, making it difficult to identify Moreton–Ramsey waves in H-alpha line core images.

3.2. Coronal Plasma Variation

The strength of the global EUV wave shock was examined by tracking the evolution of the intensity of the 193 Å passband within the region highlighted in Figure 1 (see Long et al. 2015). Assuming that the shock wave observed here is propagating perpendicular to the direction of the magnetic field (consistent with previous work, see Vršnak et al. 2002; Zhukov 2011), the magnetosonic Mach number of the wave M_{ms} can be estimated using,

$$M_{ms} = \sqrt{\frac{X(X + 5 + 5\beta)}{(4 - X)(2 + 5\beta/3)}}, \quad (1)$$

where X is the density compression ratio, defined as $X = n/n_0$, and β is the plasma- β (here assumed to be 0.1 after Muhr et al. 2011). The density compression ratio X was estimated using two different approaches; indirectly from the intensity variation in the EUV images and directly from density estimates obtained using a differential emission measure (DEM) approach.

As discussed by Zhukov (2011), the density compression ratio X can be related to the variation in intensity of the 193 Å passband via the approximation,

$$\frac{n}{n_0} = \sqrt{\frac{I}{I_0}}, \quad (2)$$

where I_0 and n_0 are the intensity and density, respectively, prior to the passage of the global wavefront. Although EUV intensity is a function of both temperature and density, this approach assumes that the change in temperature is small, enabling an estimate to be made of the change in density.

The cadence and number of passbands provided by *SDO*/*AIA* have led to the development of a variety of techniques for estimating the DEM of the coronal plasma observed by *SDO*/*AIA*.

³ See https://www.solarmonitor.org/data/2014/03/29/meta/noaa_events_raw_20140329.txt.

AIA (e.g., Hannah & Kontar 2013; Cheung et al. 2015). The DEM, $\phi(T)$, is defined as,

$$\phi(T) = n_e^2(T) \frac{dh}{dT}, \quad (3)$$

where n_e is the electron density, and enables an alternative, direct estimation of how the density and temperature of the corona vary during the passage of the global EUV wave. This can then be used to confirm the observations made using the intensity variation described in Equation (2). The regularized inversion technique developed by Hannah & Kontar (2013) was used here to examine the variation in DEM-weighted average density and temperature of the region highlighted in red in Figure 1 using the approach of Vanninathan et al. (2015). Following Cheng et al. (2012), the DEM-averaged temperature and density can be defined as,

$$T = \frac{\int \phi(T) T dT}{\int \phi(T) dT}, \quad (4)$$

and,

$$n = \sqrt{\frac{\int \phi(T) dT}{h}}, \quad (5)$$

respectively, where h is the scale height (taken here as 90 Mm following observations by, e.g., Patsourakos & Vourlidas 2009). This enabled an estimate to be made of the variation in both average temperature and density in the region of interest using the DEM derived directly from the AIA observations.

The variation in image intensity (blue), DEM-derived density (black) and DEM-derived temperature (red) are shown for each event in Figure 4. It is clear that each parameter exhibits an increase as a result of the passage of the global wave. In each case, the intensity of the 193 Å passband increases first, followed by the average density and finally the average temperature. Although the DEM-estimated average temperature exhibits an increase due to the passage of the wave, in each case the percentage increase is quite small ($\lesssim 1.1\%$). This is consistent with the work discussed by Zhukov (2011), and the weak nature of the shocks presented here, and indicates that estimating the change in image intensity as being due to the change in density (as in Equation (2)) is a valid approximation in this case. The variation in density and temperature are also consistent with the work of Vanninathan et al. (2015), although the percentage increases (decreases) in density (temperature) are much larger (smaller) than previously found.

Figure 4 also shows the magnetosonic Mach numbers using the shock compression ratio estimated by both intensity variation and DEM approaches. The Mach number estimated using the change in image intensity is consistently lower than that estimated using the DEM approach. This is most likely due to the fact that the DEM returns an estimate of the plasma distribution as a function of temperature integrated along the line of sight. All of the wavepulses studied here are propagating toward the north pole from an active region in the northern hemisphere, resulting in an increased amount of plasma along the line of sight contributing to the DEM solution. This increase in plasma along the line of sight as a function of latitudinal wave position results in an increased density value estimated using the DEM technique described here. This is a

consequence of the depth of the line-of-sight plasma contribution greatly exceeding the scale height assumed to estimate the density. However, all of the estimated Mach numbers are consistent with the previous events studied by Long et al. (2014) and Muhr et al. (2011). The small estimated Mach numbers in each case are consistent with a weakly shocked global wave (see Long et al. 2017a).

4. Discussion

The four events presented here offer a rare opportunity to investigate and quantify how a global coronal wave pulse can drive a Moreton–Ramsey wave in H-alpha observations. The four events originate from the same active region over the course of ≈ 42 hr and can be considered to be homologous, with comparable geometry, kinematics, and evolutionary behavior. Although quite fast, none of the four events were particularly strong, with Mach numbers of ≈ 1.03 – 1.20 (depending on technique used to estimate them). This is comparable to previously studied events (e.g., Long et al. 2015), none of which produced Moreton–Ramsey waves, suggesting an additional requirement is needed in order to produce a response in the H-alpha line core observations discussed here.

Simulations performed by Vršnak et al. (2016) suggested that a chromospheric response in H-alpha observations could be induced by a sufficiently strong density perturbation propagating in the corona. In this scenario, the density perturbation is produced by the rapid overexpansion of an impulsive erupting flux rope, which acts as a subsonic piston and drives a large-amplitude simple wave that can then shock and produce the observed global coronal wave. If the perturbation is sufficiently strong in the low corona at heights ≤ 100 Mm (in this case with both a Mach number M_A and density compression ratio $X = n_1/n_2$ of ≈ 2), the downward propagation of the plasma flow induces a chromospheric signature observed as the Moreton–Ramsey wave. As shown in Figure 4, the density compression ratios and Mach numbers estimated for each of the events presented here are much lower than those predicted by Vršnak et al. (2016), yet in each case a Moreton–Ramsey wave is observed. Given the inevitable complications when comparing idealized simulations with real observations, there are several possible solutions for this discrepancy that require discussion.

The first issue here is that the global waves observed here originate in an active region located at $\approx N10^\circ$ and propagate toward the north solar pole. As a result, there are increased foreshortening effects that must be accounted for when considering each event. The estimated density compression ratio and Mach numbers should therefore be considered to be a minimum estimate of the true values. While it is true that the numbers given here are at the lower end of previous observations (for example, those presented by Muhr et al. 2011; Long et al. 2015), all of these previously observed density compression ratios are much lower than those predicted by Vršnak et al. (2016) from simulations, suggesting that this explanation is insufficient.

An alternative explanation is that in addition to the lateral expansion of the global waves observed here, they had a much stronger downward component than previously observed events (see Warmuth et al. 2004b). As noted by Vršnak et al. (2016), it would be possible for a highly asymmetric but weakly impulsive eruption to produce a Moreton–Ramsey

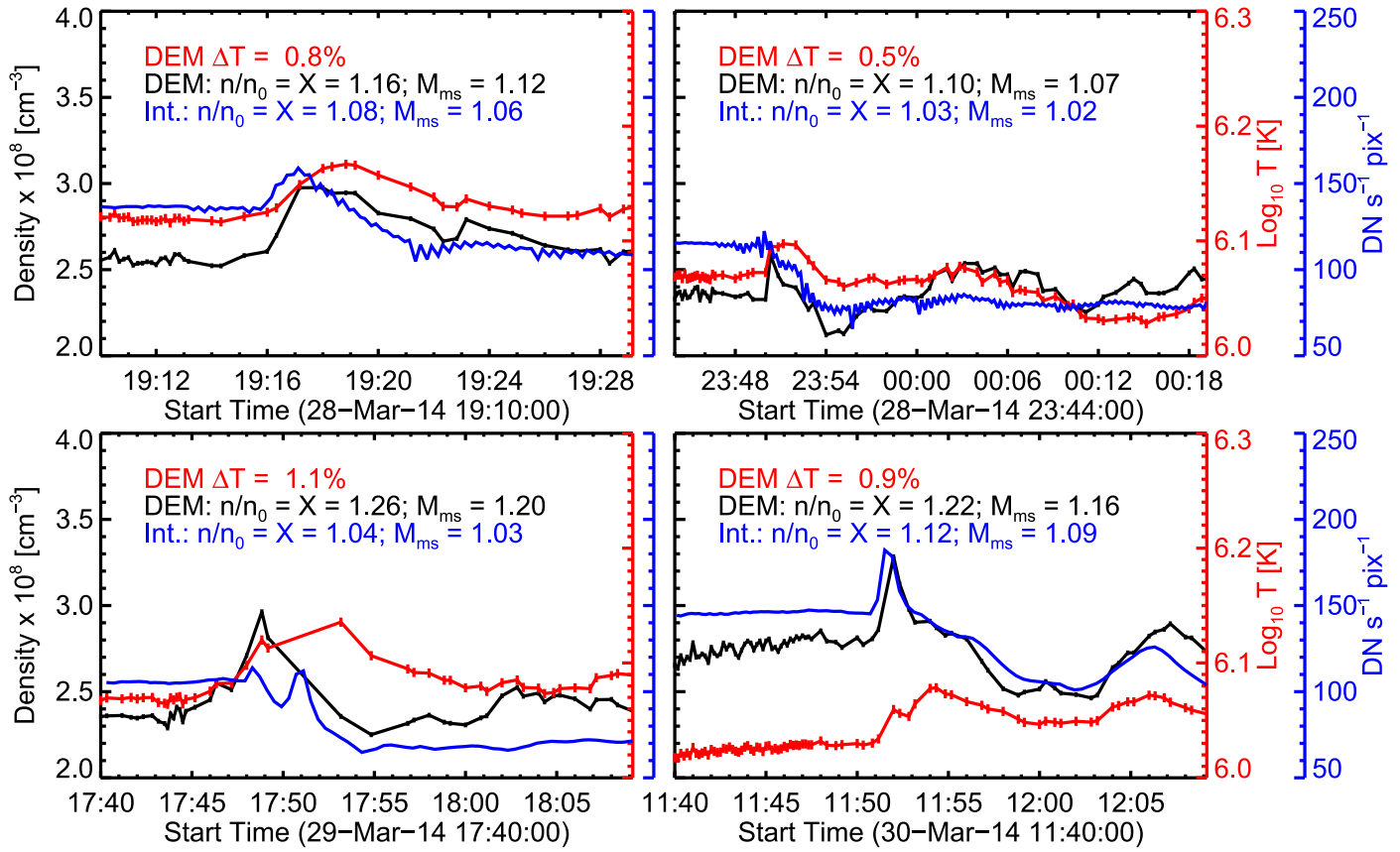


Figure 4. Variation in AIA 193 Å intensity (blue), and both density (black) and temperature (red) estimated using the DEM technique of Hannah & Kontar (2013) with time for each of the events studied here. In each case the measurements were made at the location highlighted in red in Figure 1. The legend lists the percentage increase in density and temperature, the ratio of peak image intensity to the image intensity prior to the passage of the global wave, and the magnetosonic Mach number estimated using Equation (1).

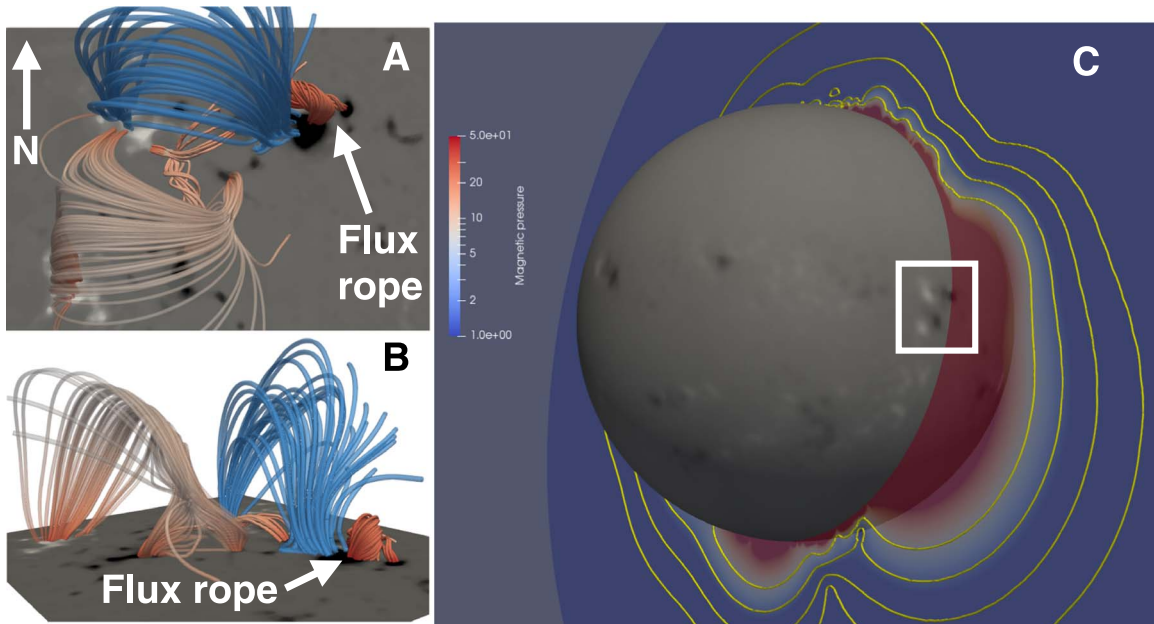


Figure 5. Zoom-in of the magnetic field of AR 12017 on 2014 March 29 using a nonlinear extrapolation from above (panel (a)) and the side (panel (b)), with the red/blue/white field lines indicating different domains of magnetic field. Panel (c) shows the calculated magnetic pressure in arbitrary units of $\approx 3.5 \times 10^{-10} \text{ dyne cm}^{-2}$ along the arc sector shown in Figure 1 from a PFSS extrapolation at 12:04 UT on 2014 March 28. The white square in panel (c) indicates the region of the magnetogram shown in panels (a) and (b), while the yellow contours indicate lines of constant magnetic pressure. Contrast the significant increase in magnetic pressure to the south of the erupting active region with the drop in magnetic pressure toward the north pole due to the increased magnetic complexity of the active region.

wave on the erupting side of the flux rope. This is consistent with the observations shown in Figure 1, where each of the global wave events can be seen to be highly asymmetric, propagating primarily toward solar north. An examination of the large-scale magnetic field in the proximity of the erupting active region (obtained using the PFSS method described by Schrijver & De Rosa 2003) and the resulting magnetic pressure shown in panel (c) of Figure 5 shows that while the magnetic pressure is quite large above and south of the erupting active region, it drops off significantly moving from the active region toward the north pole (i.e., in the direction of propagation of the global waves). This suggests that each of the eruptions could have been highly inclined as a result of following the path of least resistance, as suggested by Panasenco et al. (2013; see also the eruption from 2010 April 8 modeled by Kliem et al. 2013).

As a particularly well observed eruption event, the X1 flare on 2014 March 29 has been studied by multiple authors (see Section 1). This analysis has included several magnetic field extrapolations (see Woods et al. 2018) and spectroscopic analyses of the plasma evolution within the erupting filament before and during the flare (see Kleint et al. 2015; Woods et al. 2017). As noted in each case, for this event the eruption occurred on the northern side of the active region, and was primarily driven by flux cancellation in the middle of the active region. Global EUV waves have previously been observed to propagate asymmetrically when originating on the edges of active regions due to the increased Alfvén speed inhibiting propagation through the active region (see Long et al. 2008). This is again consistent with the increased magnetic pressure above and to the south of the erupting active region shown in Figure 5.

In addition to this, the NLFFF extrapolation in panels (a) and (b) of Figure 5 (Valori et al. 2010) confirms, first, the presence of a flux rope in the northern edge of the active region, and, second, the presence of a complex strong magnetic structure to the south of the origin of the eruption, which could also have contributed to the strongly anisotropic nature of the global wave. The large structures (seen in red and blue in panels (a) and (b) of Figure 5), would have inhibited the eruption and early evolution of the flux rope, forcing it to erupt asymmetrically toward solar north. This asymmetric eruption would have driven a global EUV wave with a significantly increased downward component, which would have pressed down on the chromosphere and been observed as a Moreton–Ramsey wave. The blue magnetic field structure also expands out above the erupting flux rope (seen as the small red structure to the top and right of panels (a) and (b) in Figure 5 respectively), which is compatible with the (current-free) large-scale structure found in the PFSS extrapolation of panel (c). Together, the two extrapolations support the conclusion that the ambient field could have contributed to the increased downward component of the global waves studied here. While the multiple eruptions would have been expected to change the topology of the surrounding magnetic field, this would be on a local rather than global scale and involves removing the currents associated with the erupting flux rope. As the PFSS is current-free, the eruptions do not affect the magnetic pressure estimated here and as a result it remains comparable to that shown in Figure 5 over the timescale discussed here.

5. Conclusions

The series of eruptions associated with AR 12017 provide a unique opportunity to study the evolution of four homologous global waves in the solar atmosphere using both EUV and H-alpha observations. Despite the long history of observations of these features, joint observations of global EUV and Moreton–Ramsey waves, particularly with very high spatial and temporal cadence, continue to be incredibly rare. Although Moreton–Ramsey waves are known to be the chromospheric footprint of a global wave propagating in the solar corona (see Uchida 1968; Warmuth 2015), far fewer observations have been made of Moreton–Ramsey waves than the regularly observed global EUV waves. However, simulations performed by Vršnak et al. (2016) suggest that the global EUV wave must be sufficiently strong for it to produce an observable perturbation of the high density chromosphere.

The events originating from AR 12017 from 2014 March 28 to 30 provide an opportunity to test this hypothesis. All four homologous waves were well observed in the corona by *SDO*/AIA and in the chromosphere by GONG, enabling a direct comparison between the events and the different regimes of the solar atmosphere. The wave kinematics were measured using multiple passbands, with the global EUV waves exhibiting high velocities and strong decelerations, consistent with previous results. The Moreton–Ramsey waves were found to have lower velocities and weaker deceleration, consistent with both the known picture of how Moreton–Ramsey waves are produced (see Warmuth et al. 2004b) and the lower cadence of the H-alpha observations (see Byrne et al. 2013).

With the kinematics of each event indicating that the global waves were weakly shocked, the density compression ratio was estimated in each case using both an intensity ratio and DEM approach. The Mach number could then be estimated for each event, with all four waves found to be very weakly shocked with Mach numbers of 1.02–1.20. Although consistent with previous work (see Long et al. 2015), these Mach numbers were below the numbers predicted from simulations by Vršnak et al. (2016), suggesting that none of the global waves should have produced a Moreton–Ramsey wave.

The magnetic structure of the erupting active region was examined to determine an alternative explanation for how each event could therefore perturb the chromosphere and produce a Moreton–Ramsey wave. It was found that each of the eruptions occurred to the north of the source active region, with the erupting flux ropes found to originate underneath an expanded magnetic loop structure. Global waves have been observed to be produced by a rapid overexpansion of the erupting flux rope, which acts as a piston and drives a shock front which then propagates freely (e.g., Patsourakos et al. 2010). However, the structure of the surrounding magnetic field found here suggests that instead of being driven laterally across the solar disk as with other events, the global wave had a significant downward component as a result of the significant asymmetric eruption of the flux rope. This therefore enabled the global EUV wave to perturb the chromosphere and produce a Moreton–Ramsey wave, despite being weaker than the limit predicted by simulations.

The authors wish to thank Julia Lawless for useful discussions and the anonymous referee for very detailed suggestions that helped clarify the manuscript. D.M.L. acknowledges support from the European Commission's

H2020 Programme under the following Grant Agreements: GRESt (No. 653982) and Pre-EST (No. 739500) as well as support from the Leverhulme Trust for an Early Career Fellowship (ECF-2014-792) and is grateful to the Science Technology and Facilities Council for the award of an Ernest Rutherford Fellowship (ST/R003246/1). G.V. was funded by the Leverhulme Trust under grant 2014-051. J.M.J. thanks the STFC for support via funding given in his PhD Studentship.

Facilities: SDO, GONG.

Software: SolarSoftWare (Freeland & Handy 1998).

ORCID iDs

David M. Long  <https://orcid.org/0000-0003-3137-0277>

Jack Jenkins  <https://orcid.org/0000-0002-8975-812X>

Gherardo Valori  <https://orcid.org/0000-0001-7809-0067>

References

- Asai, A., Ishii, T. T., Isobe, H., et al. 2012, *ApJL*, 745, L18
- Attrill, G. D. R., Harra, L. K., van Driel-Gesztelyi, L., et al. 2007, *ApJL*, 656, L101
- Balasubramaniam, K. S., Cliver, E. W., Pevtsov, A., et al. 2010, *ApJ*, 723, 587
- Byrne, J. P., Long, D. M., Gallagher, P. T., et al. 2013, *A&A*, 557, A96
- Chen, P. F., Wu, S. T., Shibata, K., et al. 2002, *ApJL*, 572, L99
- Cheng, X., Zhang, J., Saar, S. H., et al. 2012, *ApJ*, 761, 62
- Cheung, M. C. M., Boerner, P., Schrijver, C. J., et al. 2015, *ApJ*, 807, 143
- Delaboudinière, J.-P., Artzner, G. E., Brunaud, J., et al. 1995, *SoPh*, 162, 291
- Delannée, C., Hochedez, J.-F., & Aulanier, G. 2007, *A&A*, 465, 603
- Delannée, C., Török, T., Aulanier, G., et al. 2008, *SoPh*, 247, 123
- Dere, K. P., Brueckner, G. E., Howard, R. A., et al. 1997, *SoPh*, 175, 601
- Domingo, V., Fleck, B., & Poland, A. I. 1995, *SoPh*, 162, 1
- Francile, C., López, F. M., Cremades, H., et al. 2016, *SoPh*, 291, 3217
- Freeland, S. L., & Handy, B. N. 1998, *SoPh*, 182, 497
- Hannah, I. G., & Kontar, E. P. 2013, *A&A*, 553, A10
- Kaiser, M. L., Kucera, T. A., Davila, J. M., et al. 2008, *SSRv*, 136, 5
- Kienreich, I. W., Muhr, N., Veronig, A. M., et al. 2013, *SoPh*, 286, 201
- Kienreich, I. W., Veronig, A. M., Muhr, N., et al. 2011, *ApJL*, 727, L43
- Kleint, L., Battaglia, M., Reardon, K., et al. 2015, *ApJ*, 806, 9
- Kliem, B., Su, Y. N., van Ballegooijen, A. A., et al. 2013, *ApJ*, 779, 129
- Kowalski, A. F., Allred, J. C., Daw, A., et al. 2017, *ApJ*, 836, 12
- Krause, G., Cécere, M., Francile, C., et al. 2015, *MNRAS*, 453, 2799
- Krause, G., Cécere, M., Zurbriggen, E., et al. 2018, *MNRAS*, 474, 770
- Leenaarts, J., Carlsson, M., & Rouppe van der Voort, L. 2012, *ApJ*, 749, 136
- Lemen, J. R., Title, A. M., Akin, D. J., et al. 2012, *SoPh*, 275, 17
- Long, D. M., Baker, D., Williams, D. R., et al. 2015, *ApJ*, 799, 224
- Long, D. M., Bloomfield, D. S., Chen, P. F., et al. 2017a, *SoPh*, 292, 7
- Long, D. M., Bloomfield, D. S., Gallagher, P. T., et al. 2014, *SoPh*, 289, 3279
- Long, D. M., Gallagher, P. T., McAteer, R. T. J., et al. 2008, *ApJL*, 680, L81
- Long, D. M., Murphy, P., Graham, G., et al. 2017b, *SoPh*, 292, 185
- Moreton, G. E. 1960, *AJ*, 65, 494
- Moreton, G. E., & Ramsey, H. E. 1960, *PASP*, 72, 357
- Moses, D., Clette, F., Delaboudinière, J.-P., et al. 1997, *SoPh*, 175, 571
- Muhr, N., Veronig, A. M., Kienreich, I. W., et al. 2011, *ApJ*, 739, 89
- Muhr, N., Vršnak, B., Temmer, M., et al. 2010, *ApJ*, 708, 1639
- Narukage, N., Hudson, H. S., Morimoto, T., et al. 2002, *ApJL*, 572, L109
- Nitta, N. V., Schrijver, C. J., Title, A. M., et al. 2013, *ApJ*, 776, 58
- Panasenco, O., Martin, S. F., Velli, M., et al. 2013, *SoPh*, 287, 391
- Patsourakos, S., & Vourlidas, A. 2009, *ApJL*, 700, L182
- Patsourakos, S., Vourlidas, A., & Stenborg, G. 2010, *ApJL*, 724, L188
- Pesnell, W. D., Thompson, B. J., & Chamberlin, P. C. 2012, *SoPh*, 275, 3
- Polito, V., Galan, G., Reeves, K. K., et al. 2018, *ApJ*, 865, 161
- Schrijver, C. J., & De Rosa, M. L. 2003, *SoPh*, 212, 165
- Temmer, M., Vršnak, B., Žic, T., et al. 2009, *ApJ*, 702, 1343
- Thompson, B. J., Plunkett, S. P., Gurman, J. B., et al. 1998, *GeoRL*, 25, 2465
- Uchida, Y. 1968, *SoPh*, 4, 30
- Valori, G., Kliem, B., Török, T., et al. 2010, *A&A*, 519, A44
- Vanninathan, K., Veronig, A. M., Dissauer, K., et al. 2015, *ApJ*, 812, 173
- Veronig, A. M., Podladchikova, T., Dissauer, K., et al. 2018, *ApJ*, 868, 107
- Veronig, A. M., Temmer, M., Vršnak, B., et al. 2006, *ApJ*, 647, 1466
- Vršnak, B., & Cliver, E. W. 2008, *SoPh*, 253, 215
- Vršnak, B., Žic, T., Lulić, S., et al. 2016, *SoPh*, 291, 89
- Vršnak, B., Warmuth, A., Brajša, R., et al. 2002, *A&A*, 394, 299
- Wang, H., Shen, C., & Lin, J. 2009, *ApJ*, 700, 1716
- Warmuth, A. 2015, *LRSP*, 12, 3
- Warmuth, A., Vršnak, B., Aurass, H., et al. 2001, *ApJL*, 560, L105
- Warmuth, A., Vršnak, B., Magdalenic, J., et al. 2004a, *A&A*, 418, 1101
- Warmuth, A., Vršnak, B., Magdalenic, J., et al. 2004b, *A&A*, 418, 1117
- Wills-Davey, M. J., DeForest, C. E., & Stenflo, J. O. 2007, *ApJ*, 664, 556
- Woods, M. M., Harra, L. K., Matthews, S. A., et al. 2017, *SoPh*, 292, 38
- Woods, M. M., Inoue, S., Harra, L. K., et al. 2018, *ApJ*, 860, 163
- Zhang, Y., Kitai, R., Narukage, N., et al. 2011, *PASJ*, 63, 685
- Zheng, R., Jiang, Y., Yang, J., et al. 2012, *ApJ*, 747, 67
- Zhukov, A. N. 2011, *JASTP*, 73, 1096